nature communications

Article

https://doi.org/10.1038/s41467-024-54893-9

Insights into the anomalous hardness of the tantalum carbides from dislocation mobility

Received: 11 April 2024

Accepted: 25 November 2024

Published online: 04 December 2024

Check for updates

Brennan R. Watkins [1] ✉, C. Haas Blacksher [2], Alyssa Stubbers [3], Gregory B. Thompson [2,3] & Christopher R. Weinberger [1,4]

The tantalum carbides, TaC_x, have been repeatedly shown to harden dramatically with some loss of carbon content, then soften with further decarburization. First observed in 1963, this anomalous hardness behavior has been reproduced for decades without satisfactory explanation. Prior attempts to characterize this phenomenon using elastic stiffnesses have failed to reproduce the anomalous hardness behavior. In this work, we demonstrate a change in slip system preference from $\{111\}_{B1}$ to $\{110\}_{B1}$ in TaC_x as x decreases, while no such transition is observed in TiC_x. We find this to be the primary mechanism of the anomalous hardness, arising from reduced energetic favorability of dissociation of dislocations on $\{111\}_{B1}$ into Shockley partials at lower carbon contents. We also present experimental hardness measurements for bulk and thin-film TaC_x at different carbon contents. An anomalous hardness peak is observed in the bulk samples, but not in the thin films, due to loss of dislocation plasticity in the nanocrystalline films.

Indentation hardness, or a material's resistance to local plastic deformation, remains something of a challenge to researchers seeking to understand the inelastic deformation behavior of crystalline materials. Though not a material property per se, hardness provides an indispensable metric for characterizing a material's resistance to irreversible deformation under loading; furthermore, there is a vast array of engineering applications for hard materials—wear-resistant coatings, armor materials, cutting tools, etc[1–4]. The development of reliable quantitative models for hardness is hindered, however, by the dependence of a material's measured hardness on factors such as the geometry of the indenter tip, the size of the indent[5,6], and the microstructural features of the sample. Correspondingly, experimental hardness measurements can be extremely variable depending on the conditions around the indenter—such as porosity[7] and grain orientation[8,9]—and often these experimental details are not fully reported; this lack of reproducibility heightens the barrier to understanding the complex elastic and inelastic deformation processes active during an indentation event, especially as the hardness of the sample approaches that of the indenter[10].

A good illustration of this gap in scientific understanding is the persistent problem of anomalous hardness in the tantalum carbides. The transition-metal carbides (TMCs) are a much-studied class of hard materials with exceptional melting temperatures[11–13] and good low-temperature hardness[14–16]; we specifically highlight the titanium and tantalum carbides because they exhibit very different hardness changes with loss of carbon content, despite having the same metallic-covalent bonding and rocksalt (B1) crystal structure. TiC_x can be taken as representative of the IVB TMCs—that is, the carbides of the Group IVB transition metals—as its hardness declines roughly linearly with loss of carbon content. This result is intuitive, since decarburization reduces the density of covalent metal-carbon bonds within the material. In stark contrast, the VB TMCs (those carbides comprised of the Group VB transition metals) deviate significantly from this behavior; among them, TaC_x is unique in that it exhibits a sub-stoichiometric maximum hardness at a composition around $TaC_{0.83}$. Thus, bizarrely, some reduction in carbon content produces an anomalous increase in the hardness, after which further decarburization causes the hardness to decline; a comparison of this behavior with that of TiC_x is shown in

[1]Department of Mechanical Engineering, Colorado State University, Fort Collins, CO, USA. [2]Department of Metallurgical and Materials Engineering, University of Alabama, Tuscaloosa, AL, USA. [3]Alabama Materials Institute, University of Alabama, Tuscaloosa, AL, USA. [4]School of Materials Science and Engineering, Colorado State University, Fort Collins, CO, USA. ✉e-mail: brenno@colostate.edu

https://doi.org/10.1038/s41467-024-54893-9

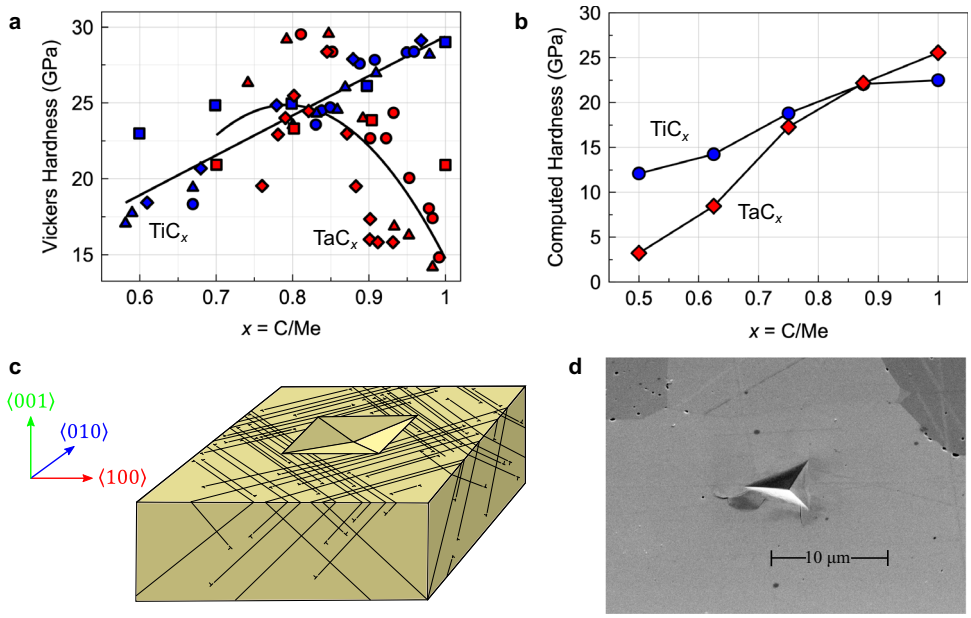

Fig. 1 | The anomalous hardness behavior of the transition-metal carbides. **a** Comparison of microhardness data aggregated by Gusev et al.[63] from prior experiments[17,64–66], showing the anomalous behavior of TaC_x (red markers) alongside the more predictable trend of TiC_x (blue markers); second-order polynomial fits are shown for both sets of data, emphasizing the difference in hardness behavior between the two carbides. **b** Predicted hardnesses for TiC_x (blue markers) and TaC_x (red markers) from elastic constants, showing no anomalous hardness behavior. **c** Illustration of a Vickers indent in a cubic carbide sample, showing traces of dislocation slip on the {111} crystallographic planes. **d** Image of a nano-indent in a bulk tantalum carbide sample, showing displaced material around the indent.

Fig. 1a. This anomalous hardness, first observed by Santoro[17] in 1963, has been consistently measured in indentation experiments.

Many predictive models of hardness which are readily applied to this problem draw upon the well-established correlation between the shear modulus of a crystal and its indentation hardness[18–22]. More generally, the search for superior hard materials largely depends upon an analysis of elastic moduli[23–25]. This association is logical, since the strength and number of interatomic bonds within a crystal will contribute to both its elastic stiffness and its resistance to plastic deformation. Furthermore, density-functional theory (DFT) calculations[26,27] have predicted maximum C_{44} stiffness values at a valence-electron concentration between 8.4 and 8.6 valence electrons per unit cell in mixed carbides and carbonitrides. However, prior ab initio work[28] has not shown the shear modulus of TaC_x to possess a sub-stoichiometric peak. Hardness predictions made using DFT-computed elastic stiffnesses and a correlational model developed by Chen et al.[29] are shown in Fig. 1b for both TiC_x and TaC_x, incorrectly predicting a general softening for both carbides with loss of carbon content. It is perhaps unsurprising that this model fails to anticipate the anomalous hardness of TaC_x, since it fundamentally overlooks the actual mechanisms of irreversible deformation. Elastic stiffness represents a material's resistance to infinitesimal bond distortions; during plastic flow, bonds undergo large deformations, break, and re-form elsewhere. For a more comprehensive view of hardness behavior, then, we must examine the principal carriers of low-temperature plastic deformation: dislocations. The motion of these one-dimensional crystallographic defects—referred to as "slip"—accommodates the irreversible shape change inflicted during indentation, as illustrated in Fig. 1c, so the mobility of dislocations should be a principal consideration when constructing a detailed model of hardness. As an example, a representative indentation in stoichiometric TaC, Fig. 1d, shows characteristic plasticity and pile-up of material around the indent.

But how does dislocation slip behavior vary among the cubic carbides? Recent computational work has indicated the presence of a metastable intrinsic stacking-fault (ISF) in TaC via examination of the $\langle 112 \rangle \{111\}_{B1}$ generalized stacking-fault (GSF) energy curve; this metastable point is absent from HfC[30]. Subsequent investigation by Yu et al.[31] has shown that all of the IVB TMCs lack a metastable ISF, while all of the VB TMCs possess one. This work also demonstrated the energetic favorability of dissociation of $\frac{a}{2}\langle 110 \rangle$ dislocations into pairs of $\frac{a}{6}\langle 112 \rangle$ Shockley partials in the VB TMCs, potentially allowing for a change in slip plane preference from $\{110\}_{B1}$ to $\{111\}_{B1}$. Such a prediction comports with hardness anisotropy (HA) experiments, wherein the IVB TMCs have been shown to slip via the $\{110\}_{B1}$ planes at low temperatures—only exhibiting $\{111\}_{B1}$ slip at high temperatures—while the stoichiometric VB TMCs are claimed to slip on the $\{111\}_{B1}$ planes even at room temperature, with significant evidence of dislocation plasticity noted in most experiments[32–35]. Prior ab initio work, however, has been limited to stoichiometric ($x = 1$) TMCs, giving no indication of how decarburization affects the slip behavior of the carbides; HA experiments generally do not vary carbon concentration between samples of a given TMC, so there is little direct evidence for variations in slip plane preference. It is worth noting that a loss of $\{111\}_{B1}$ slip availability has been proposed for TaC_x at lower carbon contents[36], but no direct observation of dislocation slip or HA has been made around the $TaC_{0.83}$ (or Ta_6C_5) composition. One possible reason for this lack of concrete information on the slip behavior of Ta_6C_5 is its more brittle behavior when compared with TaC: similar to IVB TMCs such as TiC, sub-stoichiometric TaC_x tends not to exhibit pronounced slip traces around the indent[37]. Micropillar compression tests have affirmed the presence of $\{110\}_{B1}$ slip in HfC and {111}B1 slip in TaC—as well as greatly reduced evidence of plasticity in HfC as compared to TaC—further supporting the notion that dislocation mobility is responsible for the very different hardness behaviors among the cubic carbides[38].

In this work, we use a dislocation modeling approach to identify a transition in slip plane dominance from $\{111\}_{B1}$ to $\{110\}_{B1}$ in TaC_x as x is reduced, whereas TiC_x undergoes no such transition. We thereby conclude that the anomalous hardness behavior of TaC_x arises from the loss of easy $\{111\}_{B1}$ slip at lower carbon contents; TiC_x exhibits no anomalous trend because Peierls stresses are very high at all x values sampled in this work. We also find compelling experimental evidence that dislocation slip resistance is responsible for the anomalous

https://doi.org/10.1038/s41467-024-54893-9

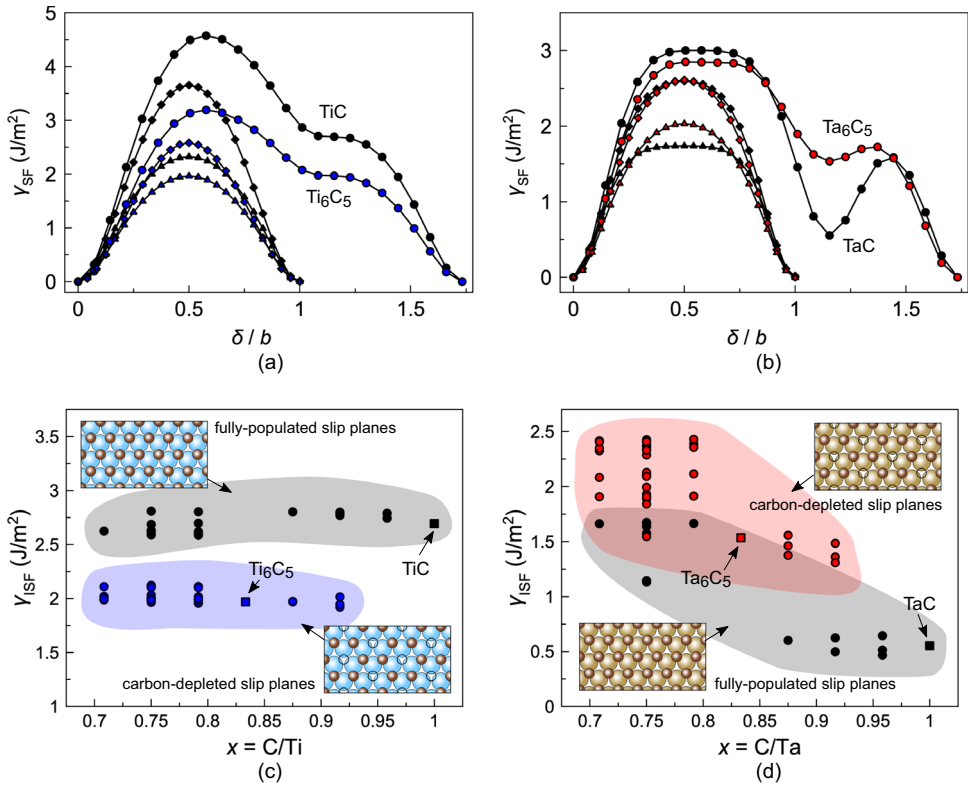

Fig. 2 | Trends in intrinsic stacking-fault energy in the carbides. DFT-computed generalized stacking-fault energy, γ_{SF}, curves for (**a**) TiC_x and (**b**) TaC_x as a function of the disregistry δ, in units of the perfect dislocation Burgers vector magnitude b (equal to $\left|\frac{a}{2}\langle 110\rangle\right| = \frac{a\sqrt{2}}{2}$, where a is the conventional B1 lattice constant), between the upper and lower half-spaces of the simulation cell. The stoichiometric MC composition is indicated by black lines and markers, while colored markers denote the M_6C_5 composition. Circle markers denote $\langle 112\rangle\{111\}_{B1}$ slip, diamond markers represent $\langle 110\rangle\{111\}_{B1}$ slip, and triangle markers represent $\langle 110\rangle\{110\}_{B1}$ slip. The variation in computed intrinsic stacking-fault energy, γ_{ISF}, at different carbon contents is shown for (**c**) TiC_x and (**d**) TaC_x, showing the effect of vacancy filling in the sub-stoichiometric structure. In both (**c**) and (**d**), black markers denote fully-populated close-packed carbon planes adjacent to the slip plane, while colored markers indicate carbon planes containing vacancies (ordered as seen in the figure insets) adjacent to the slip plane; the accompanying shaded regions are included to indicate clusters of data. Circle markers represent different structures with varying proportions of carbon-depleted planes (which may be distributed differently throughout the simulation cell), while square markers indicate the structures used to generate the MC and M_6C_5 GSF energy curves shown in (**a**) and (**b**). The insets in (**c**) and (**d**) illustrate the ordering of carbon vacancies (open circles) on the slip plane, with carbon atoms shown as brown spheres and metal atoms shown as either blue (titanium) or gold (tantalum) spheres.

hardness, showing the anomalous hardness to disappear entirely in nanocrystalline TaC_x films wherein dislocation plasticity is restricted by the high density of grain boundaries.

Results and discussion

Generalized stacking-fault energies

We computed GSF energy curves for both TaC_x and TiC_x at stoichiometric and sub-stoichiometric compositions. As seen in Fig. 2a, the sub-stoichiometric Ti_6C_5 has identical GSF curve morphology to the stoichiometric TiC; in both sets of curves, the $\langle 112\rangle\{111\}_{B1}$ shows no metastable ISF. However, Fig. 2b shows the metastable ISF seen in TaC to be present in Ta_6C_5 as well; furthermore, the ISF energy is seen to increase nearly threefold—from 0.553 to 1.535 J/m^2. Figure 2c shows no significant change in ISF energies for TiC_x, while Fig. 2d details the upward trend in computed ISF energies for TaC_x structures with decreasing x. For both materials, the variation in ISF energies at each x stems from the availability of slip planes with and without carbon vacancies. Interestingly, the fully-populated TiC_x carbon planes have similar ISF energies irrespective of composition, while the carbon-depleted planes have lower ISF energies that vary little with composition. These trends indicate decreasing favorability of dislocation dissociation on the TaC_x $\{111\}_{B1}$ crystallographic planes as carbon concentration decreases, in turn suggesting a diminished preference for $\{111\}_{B1}$ slip at lower carbon contents. In TiC_x, which can be seen as a prototype for all of the IVB TMCs, the GSF energy curves suggest no preference for $\{111\}_{B1}$ slip at any composition; this is initially consistent with previous experimental observations.

Our investigation of the sub-stoichiometric TMCs focused on vacancy-ordered M_6C_5, which can be thought of as a "superlattice" of carbon vacancies within the B1 host lattice[39]. This structure, shown in Fig. 3a, belongs to the C2/m space group and contains alternating $\{111\}_{B1}$ planes of metal and carbon atoms; half of the carbon layers are fully populated, while the other half are missing one-third of their carbon atoms. A view of the decarburized $\{111\}_{B1}$ plane in this structure is shown in Fig. 3b. Seeking to examine the effect of local carbon content on the GSF energy curves in TaC_x, we selectively added carbon to these vacancy-containing $\{111\}_{B1}$ planes in the C2/m Ta_6C_5 structure. This was accomplished simply by replacing structural carbon vacancies with carbon atoms; due to the periodic boundary conditions utilized in our simulations, the replacement of a vacancy with an atom in a given layer effectively eliminates all vacancies from that layer. As seen in Fig. 3c, the presence or absence of carbon vacancies in the slip plane (L3) largely determines the ISF energy; the filling of adjacent carbon-deficient layers (L2 and L4) has only a mild effect, whereas the carbon content of the most distant layer (L1) has a negligible effect. Furthermore, since ordering effects have been proposed as an explanation for the unusual hardness trends in the TMCs[40,41], we created an additional ordered M_6C_5 phase which has the nominal carbon content in each

https://doi.org/10.1038/s41467-024-54893-9

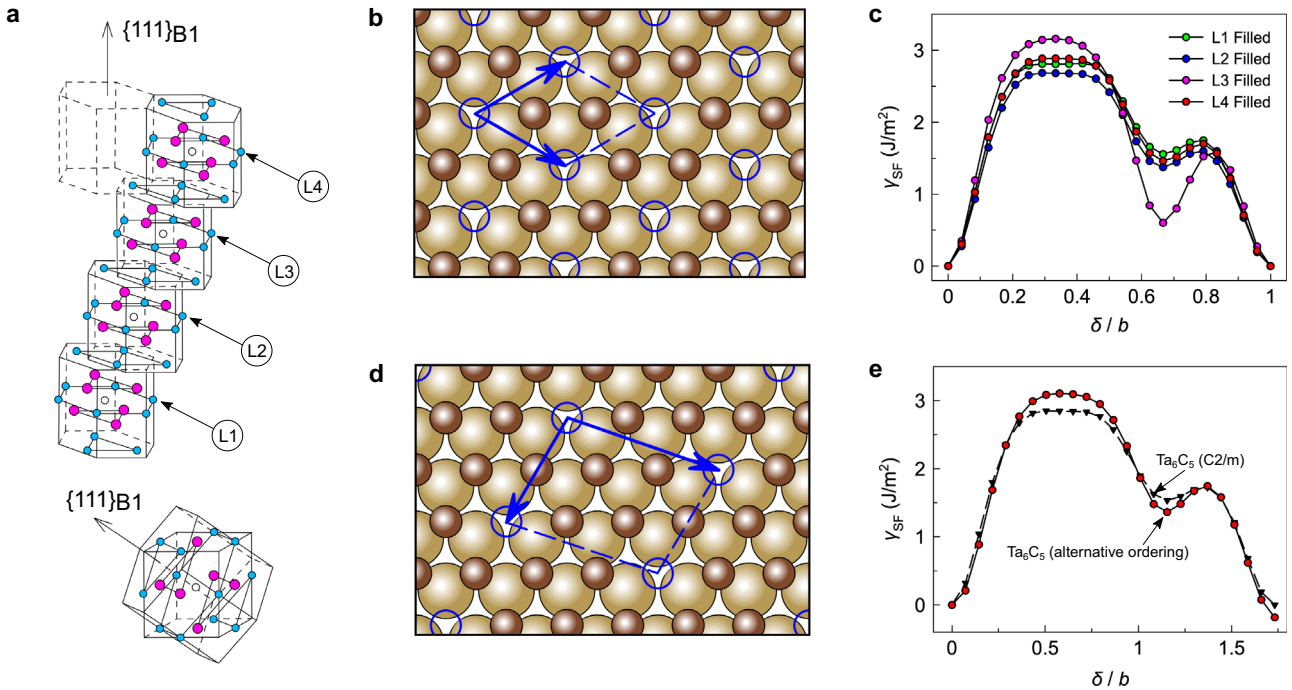

Fig. 3 | Local and global chemistry effects on stacking-fault energies. a Illustration of the primary vacancy-ordered C2/m M_6C_5 structure investigated in this work, with the position of an M_6C_5 quasi-molecule within the host B1 structure shown below. Metal atoms are indicated by magenta markers, carbon atoms are indicated by blue markers, and empty circles represent structural carbon vacancies. The slip plane for the shown GSF energy curves lies between L3 and the underlying metal $\{111\}_{B1}$ layer. **b** View from $\langle 111\rangle_{B1}$ direction of vacancy ordering in the structure shown in (**a**), with a representative cell defined by blue arrows. **c** Variation in $\langle 112\rangle\{111\}_{B1}$ GSF energies observed with selective filling of the carbon-depleted planes labeled in (**a**), showing relatively localized effect of vacancy filing on the ISF energy (the metastable point at the $\delta/b = 2\sqrt{3}/3$ location on each curve). All disregistry values are shown in units of the perfect dislocation Burgers vector magnitude b. **d** View from $\langle 111\rangle_{B1}$ direction of vacancy ordering in the alternative-ordered M_6C_5 structure. **e** GSF energy curve for $\langle 112\rangle\{111\}_{B1}$ in M_6C_5 with alternative vacancy ordering, showing little variation in ISF energy due to particular ordering of carbon vacancies.

$\{111\}_{B1}$ plane (see Fig. 3d). The $\langle 112\rangle\{111\}_{B1}$ GSF energy curve for this phase, shown in Fig. 3e, illustrates the minimal effect of ordering on the important features of the curve; specifically, the ISF exhibits the same elevated energy when compared to TaC, only differing from that of the C2/m phase by about 171 mJ/m^2. Furthermore, the reduced in-plane symmetry—compare Fig. 3b–d—of this ordered structure implies that $\frac{a}{2}\langle 112\rangle$ is no longer a primitive translation vector for the unit cell, resulting in the nonzero energy at the rightward end of the GSF energy curve. It should be noted that, if this energy difference is accounted for, the ISF energy becomes nearly identical to that seen in the $\langle 112\rangle\{111\}_{B1}$ C2/m Ta_6C_5 curve. On the whole, these results strongly imply that the ISF energy increase between TaC and Ta_6C_5 is essentially independent of ordering effects, and furthermore depends most strongly on the presence of vacancies proximal to the shear plane. It should be noted that some prior work has identified migration of nonmetal vacancies to stacking-faults as a possible pinning mechanism in some of the carbides and nitrides[42–45], owing to very low carbon diffusion rates at room temperature. Likewise, nonmetal vacancies have been identified as possibly impeding dislocation motion in ionic ceramics due to local lattice distortions[46–48] despite low Peierls stresses. However, we expect these effects to be minimal in the carbides: though vacancies may condense onto stacking-faults on grown-in dislocations, and thereby arrest their motion, a far greater number of unpinned dislocations will be nucleated during indentation. These materials are found to have low diffusion rates in computational studies[49], and low diffusion rates can also be inferred from their generally low creep rates at high temperatures[50,51]; this will then prevent carbon vacancies from attaching to freshly nucleated dislocations, meaning that this effect will likely be negligible once any significant amount of irreversible deformation has occurred.

Peierls–Nabarro dislocation model

To gain insight into the dislocation slip differences between TiC_x and TaC_x, we computed Peierls stresses, τ_P, for both materials using a semi-discrete variational Peierls–Nabarro model (SVPN)[52] similar to that used by Liu et al.[53,54] for slip characterization in FCC metals. Unlike this prior work, we broadened our investigation to include both $\{111\}_{B1}$ and $\{110\}_{B1}$ slip systems. Compositions between the bounding M_6C_5 and MC phases were modeled using interpolated GSF energies, lattice parameters, and elastic stiffnesses (see Figs. S1, S2 and S6 in the Supplementary Information for further details). The Peierls stresses obtained using this approach represent the intrinsic resistance of the lattice to dislocation slip on specific crystallographic planes, allowing us to observe changes in dislocation mobility with loss of carbon content in the absence of extrinsic effects on hardness (porosity, grain size, etc.). As Fig. 4a, b illustrates, the Peierls stresses for TaC_x rise dramatically on $\{111\}_{B1}$ as carbon vacancies are introduced; this causes the $\tau_P^{\{111\}}$ values to exceed the $\tau_P^{\{110\}}$ values at a composition around $x = 0.92$. No such transition occurs in TiC_x as the $\{111\}_{B1}$ Peierls stresses are uniformly much greater (by roughly an order of magnitude) than the $\{110\}_{B1}$ Peierls stresses. Hence, we can reasonably conclude that a change of slip system dominance—from $\{111\}_{B1}$ to $\{110\}_{B1}$—occurs in TaC_x as carbon is lost, resulting in a significant reduction in dislocation mobility. In TiC_x, however, we see the expected monotonic decline in effective intrinsic slip resistance—as determined by the Peierls stress of the lowest-stress slip plane—with loss of carbon content. To further assess the reasonableness of these changes, we can compare the magnitude of the intrinsic slip resistance increase or decrease between our bounding compositions. Going from TiC to $TiC_{0.83}$, we see a roughly 24% decrease in effective intrinsic slip resistance; in TaC_x, the same composition change produces a roughly 61% increase in intrinsic

https://doi.org/10.1038/s41467-024-54893-9

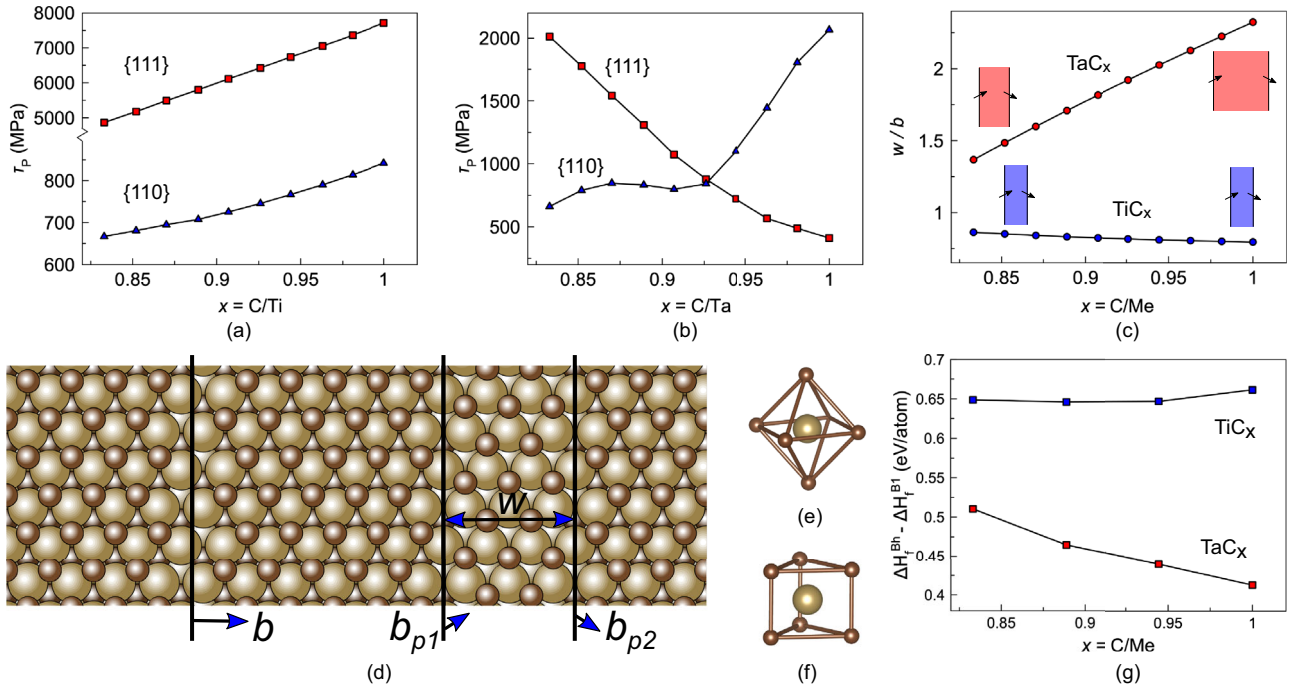

Fig. 4 | Availability of $\{111\}_{B1}$ slip in TiC_x and TaC_x. Computed Peierls stresses for **a** TiC_x and **b** TaC_x on the $\{111\}_{B1}$ and $\{110\}_{B1}$ slip planes, with red squares indicating $\{111\}_{B1}$ and blue triangles indicating $\{110\}_{B1}$. **c** Computed stacking-fault widths, w, for TiC_x and TaC_x at different carbon contents. Narrow and wide stacking-faults, bounded by partial dislocations, are indicated by the figure insets: blue for TiC_x and red for TaC_x. **d** Dissociation of an edge dislocation with perfect Burgers vector b into a pair of Shockley partial dislocations with Burgers vectors b_{p1} and b_{p2} in a B1 crystal, showing an intrinsic stacking-fault formed between the partials. **e** The octahedral coordination environment seen in the B1 crystal. **f** The trigonal prismatic coordination environment of the B_h crystal. **g** The energy difference between B_h and B1 structures in TiC_x (blue markers) and TaC_x (red markers).

slip resistance. The maximum effective intrinsic slip resistance in TaC_x occurs at a slightly higher carbon content than indicated by experimental hardness data—about $x = 0.87$, as opposed to 0.84—and indicates a roughly 106% increase in τ_P when compared to stoichiometric TaC. In both cases, the changes are slightly overestimated when compared with actual hardness data; nonetheless, the SVPN result indicates a reduction in dislocation mobility in TaC_x at lower carbon contents, consistent with experimental observations of enhanced hardness. Additionally, the $\{111\}_{B1}$ planes are independently capable of satisfying the von Mises criterion for general plasticity (which requires five independent slip systems to be active), whereas the $\{110\}_{B1}$ are insufficient to satisfy this criterion. Hence, the rapid increase in Peierls stress on the $\{111\}_{B1}$ planes will leave an insufficient number of high-mobility slip planes at reduced carbon contents, leading to a reduction in dislocation plasticity and generally more brittle behavior.

Per our earlier discussion of GSF energy curve morphology, we anticipated that greater spatial separation of Shockley partials (i.e., greater stacking-fault width) on $\{111\}_{B1}$ would yield greater dislocation mobility, as the partial dislocations (owing to their smaller Burgers vector magnitudes and consequently smaller stress fields) may be more mobile—even as a pair bounding a stacking-fault—than an undissociated dislocation. This is theoretically sound, since the motion of each partial represents a much more modest change in the local ordering of the lattice than does the motion of the original dislocation; furthermore, the growth of the stacking-fault by the movement of the leading Shockley partial is energetically balanced by the elimination of some stacking-fault area as the trailing Shockley partial moves. From our Peierls stress estimates, we can now actually quantitatively link the ISF energy change to the mobility of dislocations on the $\{111\}_{B1}$ planes. Figure 4c shows the variation in stacking-fault width, w, in TiC_x and TaC_x for $0.83 \le x \le 1.0$; it is clear that w exhibits a fairly pronounced decrease with decreasing x, affirming that the reduced ISF energy in TaC allows for increased dissociation of dislocations on $\{111\}_{B1}$. For TiC_x, w shows relatively little variation between TiC and Ti_6C_5. The w values are also quite small—less than one Burgers vector magnitude—implying that no meaningful change in $\{111\}_{B1}$ slip resistance occurs over this composition range in TiC_x. An illustration of Shockley partial and ISF formation in TaC is shown in Fig. 4d for clarity.

B1 vs. B_h structural energy differences

On the whole, these results indicate that the rapid rise in ISF energy with decreasing x produces a dramatic reduction in dislocation mobility on $\{111\}_{B1}$ planes in TaC_x, giving good evidence that the "anomalous" hardness of $TaC_{0.83}$ is produced by a loss of $\{111\}_{B1}$ slip availability. Since a stacking-fault in the B1 structure, Fig. 4e, produces a local transition to the α-WC structure (B_h), Fig. 4f, the ISF energy can be thought of as the structural energy difference between B1 and B_h. As is seen in Fig. 4g, the energetic preference for B1 over B_h is low in stoichiometric TaC, allowing for easy stacking-fault formation; in $TaC_{0.83}$, as in TiC_x at any x, the energy penalty associated with a local phase change to B_h is much higher. This means that the additional valence electron present in TaC reduces the preference for octahedral coordination of atoms within the crystal by lowering the energy of the trigonal prismatic coordination environment seen in the B_h structure. A further increase in the valence electron number (as seen in WC and the VB nitrides) stabilizes the B_h structure relative to the B1 structure, resulting in a negative ISF energy[31]. As carbon is removed from TaC_x, then, this additional valence electron charge density is gradually lost. The effective Peierls stress then increases dramatically, reducing the material's plasticity and causing TaC_x to behave more like the IVB carbides at lower x values.

Indentation hardness measurements in TaC_x

If these conclusions are correct, then we should expect to observe the "anomalous" hardness trend only in samples with sufficiently large grains to accommodate dislocation plasticity. We collected

https://doi.org/10.1038/s41467-024-54893-9

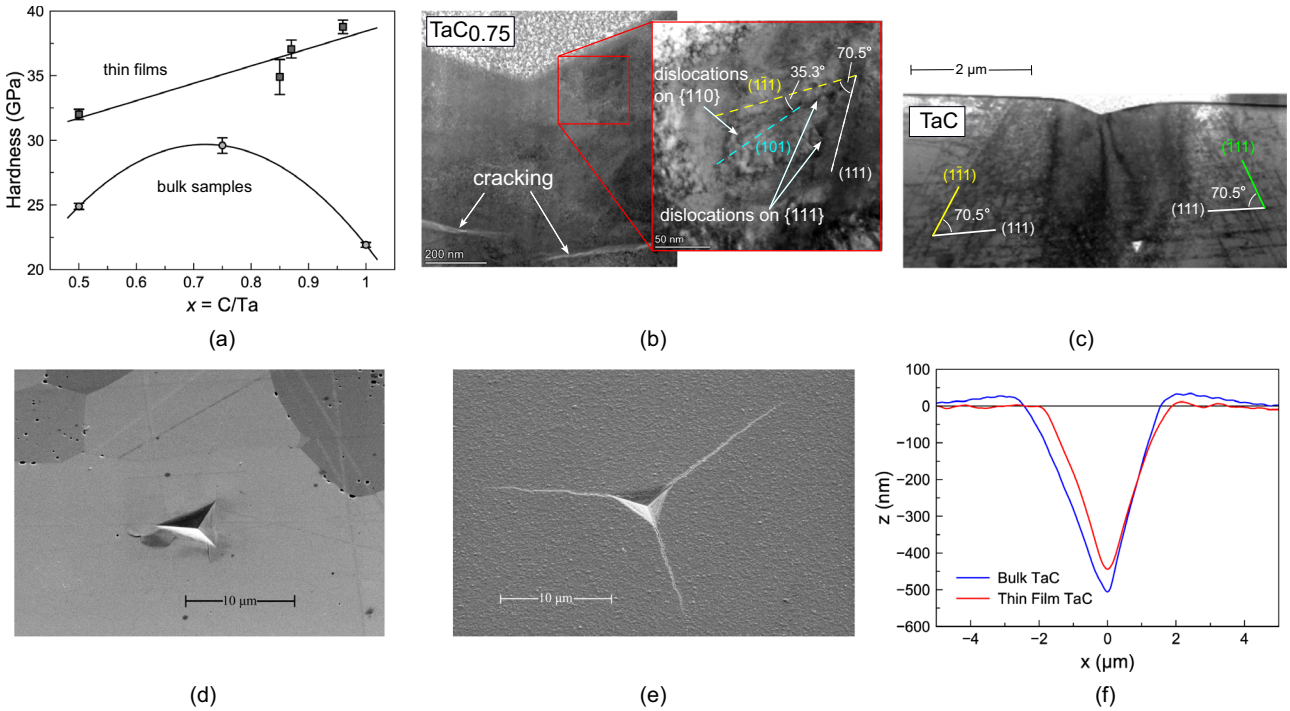

Fig. 5 | Dislocation mobility effects on the anomalous hardness of tantalum carbides. a Comparison of nanoindentation hardness measurements for bulk (circle markers) and thin-film (square markers) TaC_x at different x. Each datum represents the mean value for 50 indentation tests on a single sample, with included error bars indicating the standard error for each sample. **b** TEM image of indented bulk $TaC_{0.75}$ sample, showing significant cracking, and with slip on $\{110\}_{B1}$ and $\{111\}_{B1}$ planes evident from the angular separation of dislocations on intersecting planes (dashed guide lines offset from the dislocations so as not to obscure the dislocations). **c** TEM image of indented bulk TaC, showing abundant evidence of intersecting dislocations on the close-packed $\{111\}_{B1}$ planes. **d** SEM image of a nano-indent in a coarse-grained bulk TaC sample, showing signs of pile-up. **e** SEM image of a nano-indent in a nanocrystalline TaC thin film, showing cracking along indenter edges and no pile-up. **f** Atomic force microscopy measurements of the surfaces of indented bulk and thin-film TaC samples, confirming the lack of significant pile-up in the nanocrystalline film.

experimental hardness measurements of TaC_x in both coarse-grained bulk samples and nanocrystalline thin films with varying x, Fig. 5a. In the bulk samples, which had an average grain size of 14.7 μm, we observed a modest sub-stoichiometric peak hardness; in the thin films, where the average grain size was only 25.1 nm, no such phenomenon was observed. These results are consistent with Hall–Petch breakdown in the thin films[55] due to extremely small grain size: as the grain structure becomes very fine, dislocation plasticity is no longer an available mechanism for deformation, and the drop in $\{111\}_{B1}$ slip resistance has essentially no impact on the measured hardness. Hence we see the TaC thin film behaves like a TiC bulk sample, i.e., exhibiting a linear increase in hardness with increasing carbon content. The bulk TaC_x samples, in contrast, have sufficiently coarse grain structures for dislocations to nucleate and move during indentation, and so dislocation plasticity effects play an important role in the observed hardness behavior. Thus, the "anomalous" increase in hardness with some loss of carbon content is observed between the TaC and $TaC_{0.75}$ samples, consistent with prior experimental findings. It should be noted, of course, that the precise location of the sub-stoichiometric hardness cannot be determined from only three samples. In prior work, the location of the peak differs between experiments—see Fig. 1a—and likely varies according to extrinsic hardening effects such as grain size and porosity. These results nonetheless unambiguously demonstrate a significant rise in hardness with some loss of carbon content in the bulk TaC_x, and there is good reason to believe that this behavior arises because of dislocations. Examination of an indented bulk $TaC_{0.75}$ sample, Fig. 5b, via transmission electron microscopy (TEM) yields sparse evidence of dislocation slip and significant cracking; what dislocations can be seen in the TEM image are found to slip on both $\{110\}_{B1}$ and $\{111\}_{B1}$ planes, evident from their angular separation. Figure 5c shows an array of long, straight dislocations nucleated under an indent in a bulk stoichiometric TaC sample, with slip on the $\{111\}_{B1}$ planes again evident from the 70.5° angular separation of the dislocations. Furthermore, Fig. 5d shows a bulk TaC indent with signs of pile-up around the indent—clear evidence of dislocation plasticity—whereas the indented thin film, Fig. 5e, exhibits plentiful cracking and no discernible pile-up. Further examination of the indented specimens using atomic force microscopy, Fig. 5f, confirms this observation, with the bulk sample showing characteristic pile-up of material around the indent and the nanocrystalline film showing negligible pile-up. These results are entirely consistent with the SVPN model results, indicating that dislocation mobility is the fundamental mechanism of the "anomalous" hardness trends seen in bulk TaC_x samples. Thus, we conclude that the anomalous hardness increase observed in the sub-stoichiometric tantalum carbides is the result of a change in slip plane preference from $\{111\}_{B1}$ to $\{110\}_{B1}$, stemming in turn from reduced energetic favorability of dislocation dissociation into Shockley partials on the $\{111\}_{B1}$ crystallographic planes.

Methods

Ab initio calculations

Lattice constants, formation enthalpies, elastic stiffnesses, and GSF energies were determined via DFT calculations using the Vienna Ab-initio Simulation Package. These calculations utilized the projector-augmented wave method[56], with the generalized-gradient approximation parameterized by Perdew, Burke, and Ernzerhof[57]. Ti and Ta were, respectively, modeled using the four-electron ($4s^23d^2$) and five-electron ($6s^25d^3$) pseudopotentials; in the case of C, four electrons ($2s^22p^2$) were explicitly modeled. A plane-wave cutoff energy of 500 eV was chosen for all VASP simulations. Formation enthalpy and GSF

energy estimates were obtained from structural relaxations, which were considered to be fully converged when the change in total energy between two ionic relaxation steps was less than 1×10^{-5} eV. For the formation enthalpy and elastic modulus calculations, an automatically-generated k-point mesh was used to integrate reciprocal space; in the case of the GSF energy simulations, a $N \times N \times 1$ Monkhorst-Pack[58] mesh was used, where N is an integer. The maximum k-point spacing was set to ~$2\pi \cdot 0.0171$ Å^{-1} for all VASP simulations. For the GSF energy calculations, a vacuum gap of 15 Å was created normal to the shear plane in order to prevent the stacking-fault from having non-negligible interactions with its periodically-reproduced multiples above and below the simulation cell[59]. Elastic constants were computed using simulation cells with 16 atomic positions (8 metal and 8 carbon), with varying occupation of sites on the carbon sublattice to accommodate different compositions (see Fig. S1 in the Supplementary Information). For GSF energy calculations, cells with 48 atomic sites (24 metal and 24 carbon) were used; for stoichiometric TiC and TaC, all metal and nonmetal sites were occupied, while 1/6 of nonmetal sites were left unoccupied in the Ti_6C_5 and Ta_6C_5 structures in order to produce the structural vacancies. A representative simulation cell used for GSF energy calculations can be seen in Fig. S17 in the Supplementary Information. All sub-stoichiometric GSF energy curves used to parameterize the SVPN model were computed using the M_6C_5 structure shown in Fig. 3a, owing to the very minor change in GSF energies with different vacancy ordering shown in Fig. 3d. This structure was also used for electronic structure analysis (shown in Supplementary Figs. 18–21); the optimized unit cell geometry and atomic coordinates can be found in Supplementary Dataset 1.

Semi-discrete variational Peierls–Nabarro model

GSF energies, lattice parameters, and elastic moduli from VASP were used to parameterize a two-dimensional SVPN model. This model determines the equilibrium slip distribution $\boldsymbol{\delta}(x)$ (represented in Supplementary Fig. 3) by minimizing the total dislocation energy, which is given by:

$$E_{\text{disl.}}[\boldsymbol{\delta}(x)] = \int\int \frac{\mathrm{d}\boldsymbol{\delta}(x')}{\mathrm{d}x}\frac{H}{x-x'}\boldsymbol{\delta}(x)\,\mathrm{d}x\,\mathrm{d}x' + \int \gamma[\boldsymbol{\delta}(x)]\,\mathrm{d}x - \sum_{j=1}^{3}\int \tau_j \cdot \delta_j(x)\,\mathrm{d}x$$

where x and x' are the position within the model and the positions of all infinitesimal dislocations, respectively. Here, H is the 2nd-order Stroh tensor[60] computed from the elastic moduli of the material, and the misfit potential $\gamma[\boldsymbol{\delta}(x)]$ is computed using the DFT-computed GSF energies (as shown in Supplementary Figs. 4 and 5). The τ_j are the components of the applied shear stress, resolved onto the three spatial coordinate directions. The SVPN simulation cell size was chosen to be 200×200 nearest-neighbor atomic spacings, and Peierls stresses were determined via a bisection routine. Further details on the specific implementation of the SVPN model are given in the Supplementary Information.

Though prior work by Yadav et al.[61] has sought to obtain Peierls stress estimates directly from DFT, the periodic boundary conditions necessarily present in programs such as VASP render the task of modeling an isolated dislocation in an otherwise defect-free crystal essentially impossible. For our investigation, specifically, the expectation that dislocations on some crystallographic planes might dissociate and form stacking-faults would necessitate a very large simulation cell, making a direct DFT simulation approach prohibitively expensive. This problem is compounded by the fact that we sought to model dislocations in sub-stoichiometric carbides whose longer-range symmetry would require much larger simulation cells than those employed by Yadav et al. Thus, a hierarchical modeling approach was chosen instead.

Tantalum carbide sample synthesis

The bulk TaC_x samples were made from TaC and Ta powders, hot isostatically pressed at 205 MPa in an Ar atmosphere at 1873 K for 100 min. The TaC_x thin films were reactive sputter deposited from 99.95 at.% tantalum targets in an AJA ACT Orion 3 magnetron-sputtering system using ethylene (C_2H_4) gas as a carbon source. Each film was sputtered to a thickness of ~4 μm onto a 300 μm thick [100] Si substrate with a 100 nm oxide layer on its surface. More details regarding the synthesis of tantalum carbide samples can be found in the Supplementary Information.

Tantalum carbide sample characterization

X-ray diffraction (XRD) was used for phase identification with the B1 lattice peak shift compared to literature to verify carbon concentration. In the stoichiometric TaC billet, grain size was measured from the SEM micrograph using the line-intercept method; the stoichiometric TaC thin film grain size was measured from the XRD Scherrer analysis. Hardness measurements were made with an Agilent Nano Indenter G200 equipped with a Berkovich diamond tip indenter. Test loads ranged from 70 to 640 mN to achieve an indentation at a maximum depth of 1000 nm.

A site-specific focused ion beam milling lift-out procedure[62] was used to extract the TEM foils from the indent locations whereupon they were imaged either in a Tecnia F20 (Scanning) TEM operated at 200 keV or field emission Apreo SEM at 20 keV.

Additional images and characterization details can be found in the Supplementary information.

Data availability

The raw data used to generate all figures and supplementary figures in this study are available in the Source Data file. These data, along with optimized atomic positions for the C2/m M_6C_5 structure used in this study, have also been deposited in the Mendeley Data online data repository and can be found https://data.mendeley.com/datasets/p8smwyw34b/1. Source data are provided with this paper.

Code availability

The code developed for this work is available on the Code Ocean code-sharing platform (DOI: 10.24433/CO.0658399.v1).

References

1. Wuchina, E., Opila, E., Opeka, M., Fahrenholtz, B. & Talmy, I. UHTCs: ultra-high temperature ceramic materials for extreme environment applications. *Electrochem. Soc. Interface* **16**, 30–36 (2007).
2. Kaner, R. B., Gilman, J. J. & Tolbert, S. H. Designing superhard materials. *Science* **308**, 1268–1269 (2005).
3. Kanyanta, V. *Microstructure-Property Correlations for Hard, Superhard, and Ultrahard Materials* (Springer, 2016).
4. Ball, P. Why is boron so hard? *Nat. Mater.* **9**, 6–6 (2010).
5. Pharr, G. M., Herbert, E. G. & Gao, Y. The indentation size effect: a critical examination of experimental observations and mechanistic interpretations. *Annu. Rev. Mater. Res.* **40**, 271–292 (2010).
6. Nino, A., Tanaka, A., Sugiyama, S. & Taimatsu, H. Indentation size effect for the hardness of refractory carbides. *Mater. Trans.* **51**, 1621–1626 (2010).
7. Chen, Z., Wang, X., Atkinson, A. & Brandon, N. Spherical indentation of porous ceramics: elasticity and hardness. *J. Eur. Ceram. Soc.* **36**, 1435–1445 (2016).
8. Tang, P. et al. Influence of grain orientation on hardness anisotropy and dislocation behavior of AlN ceramic in nanoindentation. *Ceram. Int.* **47**, 20298–20309 (2021).

9. Csanádi, T., Bl'anda, M., Chinh, N. Q., Hvizdoš, P. & Dusza, J. Orientation-dependent hardness and nanoindentation-induced deformation mechanisms of WC crystals. *Acta Mater.* **83**, 397–407 (2015).
10. Brazhkin, V. et al. What does 'harder than diamond' mean? *Nat. Mater.* **3**, 576–577 (2004).
11. Cedillos-Barraza, O. et al. Investigating the highest melting temperature materials: a laser melting study of the TaC-HfC system. *Sci. Rep.* **6**, 37962 (2016).
12. Eswarappa Prameela, S. et al. Materials for extreme environments. *Nat. Rev. Mater.* **8**, 81–88 (2022).
13. Hong, Q.-J. & Van De Walle, A. Prediction of the material with highest known melting point from ab initio molecular dynamics calculations. *Phys. Rev. B* **92**, 020104 (2015).
14. Sarker, P. et al. High-entropy high-hardness metal carbides discovered by entropy descriptors. *Nat. Commun.* **9**, 4980 (2018).
15. Kiani, S., Yang, J. & Kodambaka, S. Nanomechanics of refractory transition-metal carbides: a path to discovering plasticity in hard ceramics. *J. Am. Ceram. Soc.* **98**, 2313–2323 (2015).
16. Hu, J. et al. Superhard bulk high-entropy carbides with enhanced toughness via metastable in-situ particles. *Nat. Commun.* **14**, 5717 (2023).
17. Santoro, G. Variation of some properties of tantalum carbide with carbon content. *Trans. Metall. Soc. AIME* **227**, 1361–1368 (1963).
18. Teter, D. M. Computational alchemy: the search for new superhard materials. *MRS Bull.* **23**, 22–27 (1998).
19. Avery, P. et al. Predicting superhard materials via a machine learning informed evolutionary structure search. *npj Comput. Mater.* **5**, 89 (2019).
20. Allahyari, Z. & Oganov, A. R. Coevolutionary search for optimal materials in the space of all possible compounds. *npj Comput. Mater.* **6**, 55 (2020).
21. Liang, Y. et al. Enhanced hardness in transition-metal monocarbides via optimal occupancy of bonding orbitals. *ACS Appl. Mater. Interfaces* **13**, 14365–14376 (2021).
22. Liang, Y., Gao, Z., Qin, P., Gao, L. & Tang, C. The mechanism of anomalous hardening in transition-metal monoborides. *Nanoscale* **9**, 9112–9118 (2017).
23. Jin, R., Yuan, X. & Gao, E. Atomic stiffness for bulk modulus prediction and high-throughput screening of ultraincompressible crystals. *Nat. Commun.* **14**, 4258 (2023).
24. Mansouri Tehrani, A. et al. Machine learning directed search for ultraincompressible, superhard materials. *J. Am. Chem. Soc.* **140**, 9844–9853 (2018).
25. Khatri, I. et al. Correlating structure and orbital occupation with the stability and mechanical properties of 3d transition metal carbides. *J. Alloy. Compd.* **891**, 161866 (2022).
26. Jhi, S.-H., Ihm, J., Louie, S. G. & Cohen, M. L. Electronic mechanism of hardness enhancement in transition-metal carbonitrides. *Nature* **399**, 132–134 (1999).
27. Jhi, S.-H., Louie, S. G., Cohen, M. L. & Ihm, J. Vacancy hardening and softening in transition metal carbides and nitrides. *Phys. Rev. Lett.* **86**, 3348–3351 (2001).
28. Yu, X.-X., Thompson, G. B. & Weinberger, C. R. Influence of carbon vacancy formation on the elastic constants and hardening mechanisms in transition metal carbides. *J. Eur. Ceram. Soc.* **35**, 95–103 (2015).
29. Chen, X.-Q., Niu, H., Li, D. & Li, Y. Modeling hardness of polycrystalline materials and bulk metallic glasses. *Intermetallics* **19**, 1275–1281 (2011).
30. De Leon, N., Yu, X., Yu, H., Weinberger, C. R. & Thompson, G. B. Bonding effects on the slip differences in the B 1 monocarbides. *Phys. Rev. Lett.* **114**, 165502 (2015).
31. Yu, H., Bahadori, M., Thompson, G. B. & Weinberger, C. R. Understanding dislocation slip in stoichiometric rocksalt transition metal carbides and nitrides. *J. Mater. Sci.* **52**, 6235–6248 (2017).
32. Hannink, R. H. J., Kohlstedt, D. L. & Murray, M. J. Slip system determination in cubic carbides by hardness anisotropy. *Proc. R. Soc. Lond. Math. Phys. Sci.* **326**, 409–420 (1972).
33. Morgan, G. & Lewis, M. H. Hardness anisotropy in niobium carbide. *J. Mater. Sci.* **9**, 349–358 (1974).
34. Rowcliffe, D. J. & Hollox, G. E. Hardness anisotropy, deformation mechanisms and brittle-to-ductile transition in carbide. *J. Mater. Sci.* **6**, 1270–1276 (1971).
35. Kim, C., Gottstein, G. & Grummon, D. Plastic flow and dislocation structures in tantalum carbide: deformation at low and intermediate homologous temperatures. *Acta Metall. Mater.* **42**, 2291–2301 (1994).
36. Rowcliffe, D. J. & Hollox, G. E. Plastic flow and fracture of tantalum carbide and hafnium carbide at low temperatures. *J. Mater. Sci.* **6**, 1261–1269 (1971).
37. Rowcliffe, D. J. & Warren, W. J. Structure and properties of tantalum carbide crystals. *J. Mater. Sci.* **5**, 345–350 (1970).
38. Csanádi, T., Castle, E., Reece, M. J. & Dusza, J. Strength enhancement and slip behaviour of high-entropy carbide grains during micro-compression. *Sci. Rep.* **9**, 10200 (2019).
39. Venables, J. D. & Myerhoff, M. H. Ordering effects in NbC and TaC. In: *Proc. National Bureau of Standards, Solid State Chemistry*, 583–590 (1972).
40. Hannink, R. H. J. & Murray, M. J. The effect of domain size on the hardness of ordered VC0.84. *Acta Metall.* **20**, 123–131 (1972).
41. Zueva, L. V., Lipatnikov, V. N. & Gusev, A. I. Ordering effects on the microstructure and microhardness of nonstoichiometric titanium carbide TiCy. *Inorg. Mater.* **36**, 695–698 (2000).
42. Martin, J., Jouffrey, B. & Costa, P. Stacking faults in a non-stoichiometric face-centred cubic TaC. *Phys. Status Solidi B* **22**, 349–354 (1967).
43. Allison, C., Hoffman, M. & Williams, W. S. Electron energy loss spectroscopy of carbon in dissociated dislocations in tantalum carbide. *J. Appl. Phys.* **53**, 6757–6761 (1982).
44. Hoffman, M. & Williams, W. S. A simple model for the deformation behavior of tantalum carbide. *J. Am. Ceram. Soc.* **69**, 612–614 (1986).
45. Li, P. & Howe, J. Dislocation reactions in ZrN. *Acta Mater.* **50**, 4231–4239 (2002).
46. Fang, X. et al. Nanoscale to microscale reversal in room-temperature plasticity in SrTiO3 by tuning defect concentration. *Scr. Mater.* **188**, 228–232 (2020).
47. Li, Y. et al. Theoretical insights into the Peierls plasticity in SrTiO3 ceramics via dislocation remodelling. *Nat. Commun.* **13**, 6925 (2022).
48. Stich, S. et al. Room-temperature dislocation plasticity in SrTiO3 tuned by defect chemistry. *J. Am. Ceram. Soc.* **105**, 1318–1329 (2022).
49. Stotts, J. C., Thompson, G. B. & Weinberger, C. R. Modeling the diffusion-controlled phase transformations in transition metal carbide multilayer composites. *Results Eng.* **18**, 101106 (2023).
50. Martin, J., Lacour-Gayet, P. & Costa, P. Stress changes in tantalum carbide with the deformation rate and temperature (1 200 and 2 200 deg C). *Comptes Rend. Ser. C* **272**, 2127–2130 (1971).
51. Williams, W. S. Influence of temperature, strain rate, surface condition, and composition on the plasticity of transition-metal carbide crystals. *J. Appl. Phys.* **35**, 1329–1338 (1964).
52. Bulatov, V. V. & Kaxiras, E. Semidiscrete variational Peierls framework for dislocation core properties. *Phys. Rev. Lett.* **78**, 4221–4224 (1997).

53. Liu, G., Cheng, X., Wang, J., Chen, K. & Shen, Y. Atomically informed nonlocal semi-discrete variational Peierls-Nabarro model for planar core dislocations. *Sci. Rep.* **7**, 43785 (2017).
54. Liu, G., Cheng, X., Wang, J., Chen, K. & Shen, Y. Peierls stress in face-centered-cubic metals predicted from an improved semi-discrete variation Peierls-Nabarro model. *Scr. Mater.* **120**, 94–97 (2016).
55. Trelewicz, J. R. & Schuh, C. A. The Hall–Petch breakdown in nanocrystalline metals: a crossover to glass-like deformation. *Acta Mater.* **55**, 5948–5958 (2007).
56. Blöchl, P. E. Projector augmented-wave method. *Phys. Rev. B* **50**, 17953–17979 (1994).
57. Perdew, J. P., Burke, K. & Ernzerhof, M. Generalized gradient approximation made simple. *Phys. Rev. Lett.* **77**, 3865–3868 (1996).
58. Monkhorst, H. J. & Pack, J. D. Special points for Brillouin-zone integrations. *Phys. Rev. B* **13**, 5188–5192 (1976).
59. Watkins, B. R., Lopez, J. J., Yu, X.-X., Thompson, G. B. & Weinberger, C. R. The effects of mixing non-metal atoms in the B1 structured transition metal carbo-nitrides on their structure and mechanical properties: HfC1-N. *Open Ceram.* **14**, 100356 (2023).
60. Bacon, D. J., Barnett, D. M. & Scattergood, R. O. Anisotropic continuum theory of lattice defects. *Prog. Mater. Sci.* **23**, 51–262 (1980).
61. Yadav, S., Ramprasad, R., Misra, A. & Liu, X.-Y. Core structure and Peierls stress of edge and screw dislocations in TiN: a density functional theory study. *Acta Mater.* **74**, 268–277 (2014).
62. Langford, R. M. & Clinton, C. In situ lift-out using a FIB-SEM system. *Micron* **35**, 607–611 (2004).
63. Gusev, A. I., Rempel, A. A. & Magerl, A. J. *Disorder and Order in Strongly Nonstoichiometric Compounds: Transition Metal Carbides, Nitrides and Oxides* Vol. 47 (Springer Berlin Heidelberg, 2001).
64. Ramqvist, L. Variation of lattice parameter and hardness with carbon content of group 4b metal carbides. *Jernkontorets Ann.* **152**, 517–523 (1968).
65. Ramqvist, L. Variation of hardness, resistivity, and lattice parameter with carbon content of group 5b metal carbides. *Jernkontorets Ann.* **152**, 465–475 (1968).
66. Rempel, A. A., Gusev, A. I., Berger, L.-M. & Richter, V. Properties and potential areas of application. *MRS Online Proc. Libr.* **327**, 183 (1993).

Acknowledgements

This material is based upon work supported by the National Science Foundation (NSF) under Grant No. NSF-DMR-2026766 (B.R.W. and C.R.W.) and NSF-DMR-2026760 (C.H.B., A.S., and G.B.T.). This work utilized the RMACC Summit supercomputer, which was supported by NSF Award Nos. ACI-1532235 and ACI-1532236. The RMACC Summit supercomputer was a joint effort of the University of Colorado Boulder and Colorado State University. Subsequently, this work also made use of SUMMIT's successor: the RMACC Alpine supercomputer (supported by NSF Award no. 2201538), which is also a joint project of the University of Colorado Boulder and Colorado State University.

Author contributions

B.R.W. and C.R.W. carried out all first-principles calculations and implemented the Peierls–Nabarro model for the carbides. C.H.B. and G.B.T. prepared tantalum carbide samples and performed characterization, imaging, and hardness testing. A.S. conducted TEM analysis of the sub-stoichiometric tantalum carbide sample. The Article and Supplementary Information were written and edited by B.R.W., C.R.W., C.H.B., and G.B.T.

Competing interests

The authors declare no competing interests.

Additional information

Supplementary information The online version contains supplementary material available at https://doi.org/10.1038/s41467-024-54893-9.

Correspondence and requests for materials should be addressed to Brennan R. Watkins.

Peer review information *Nature Communications* thanks Chunlei Wan, Zhenping Wang, and Ruizhi Zhang for their contribution to the peer review of this work. A peer review file is available.